

# Impact of Carbon Porosity on Sulfur Conversion in Li–S Battery Cathodes in a Sparingly Polysulfide Solvating Electrolyte

Christian Kensy,<sup>[a, b]</sup> Friedrich Schwotzer,<sup>[a]</sup> Susanne Dörfler,<sup>[b]</sup> Holger Althues,<sup>[b]</sup> and Stefan Kaskel<sup>\*[a, b]</sup>

Advancing the development of lithium-sulfur (Li–S) technology is advantageous for next generation secondary batteries to improve gravimetric and volumetric energy of established energy storage devices. In this regard, a sparingly PS solvating electrolyte based on sulfolane and hydrofluoroether is known as a promising concept to enhance the volumetric energy density by increasing the cycling stability. So far, little is known about the impact of the carbon porosity on the electrochemical sulfur utilization. Herein, carbon materials with varying pore diameter and architecture (micropores, mesopores and hierarchical pores) are studied as scaffold for Li–S cathodes using TMS/TTE electrolyte to obtain more insights into the relationship between the

carbon scaffold porosity and the modified conversion mechanism of sparingly solvating electrolytes. The electrochemical evaluation under lean conditions ( $5 \mu\text{Mg}_\text{s}^{-1}$ ) revealed stable cycling performance for all Li–S cathodes. Using microporous electrodes, a reversible quasi-solid-state conversion is detected by an additional third discharge plateau being confirmed by cyclovoltammetry. GITT experiments give evidence that the carbon porosity impacts the reaction kinetics of the polysulfide conversion by using TMS/TTE electrolyte. Based on these findings, new mechanistic insights into the operation of Li–S batteries are provided by using sparingly solvating electrolytes.

## 1. Introduction

The increasing demand for efficient energy storage devices, in particular lithium-ion batteries (LIB), leads to an intensive research or development of innovative battery systems. In this regard, lithium-sulfur (Li–S) battery is a very promising candidate to overcome energy density limitations of common established LIBs. The high theoretical specific capacity ( $1672 \text{ mAh g}_\text{s}^{-1}$ ) and high theoretical energy density ( $2500 \text{ Wh kg}^{-1}$ ) enable new possibilities and advances for low-cost as well as light weight applications, e.g. drones or high altitude pseudo-satellites (HAPS).<sup>[1–3]</sup>

However, a few technological challenges still hinder a widespread industrial commercialization.<sup>[4]</sup> The central issues of the Li–S technology, especially electrolyte decomposition and anode corrosion, are related to the highly reactive metal lithium anode.<sup>[5]</sup> Further, the problem of the parasitic

polysulfide (LiPS) shuttle of liquid intermediates and thus, active material loss is related to the intrinsic solid-liquid-solid conversion mechanism.<sup>[6–8]</sup> To address these challenges several strategies, including novel polar cathode materials,<sup>[9,10]</sup> functionalized separators<sup>[11]</sup> or innovative anodes<sup>[12]</sup>, have been explored. Additionally, the volumetric energy density on cell level is another bottleneck of this battery technology due to the intrinsic low mass density of the utilized elements (sulfur and carbon). Sparingly polysulfide solvation electrolytes have the potential to overcome this issue as they enable the work under lean conditions.<sup>[13]</sup>

Mostly, studies deal with the current state-of-the-art ether-based electrolyte, comprising 1 M lithium bis(trifluoromethane-sulfonyl)imide (LiTFSI) conductive salt dissolved in 1,2-dimethoxyethane (DME) and 1,3-dioxolane (DOL) in equal volumetric ratio.<sup>[4,6,14]</sup> This electrolyte results in a catholyte-type battery system with high LiPS solubility and thus, active material is almost completely dissolved. Consequently, the resulting intermediates can easily migrate to the Li anode inducing LiPS shuttle mechanism.<sup>[8,15]</sup> In order to counteract this shuttle phenomenon, LiNO<sub>3</sub> is used as additive to improve the formation of the solid electrolyte interphase (SEI) on anode side and leads to an enhanced cycle stability or Coulombic efficiency (CE).<sup>[16]</sup> The major drawback of the LiNO<sub>3</sub> salt is its continuous consumption including gas formation, cell inflation, and consumption during cycling.<sup>[17]</sup>

Moreover, due to the high solubility of the LiPS intermediates the total electrolyte amount is directly connected to the sulfur utilization and cycle life in DME/DOL

[a] C. Kensy, F. Schwotzer, Prof. Dr. S. Kaskel  
Department of Inorganic Chemistry I  
Technische Universität Dresden  
Bergstraße 66, 01069 Dresden, Germany  
E-mail: Stefan.Kaskel@tu-dresden.de

[b] C. Kensy, Dr. S. Dörfler, Dr. H. Althues, Prof. Dr. S. Kaskel  
Department of Surface and Battery Technology  
Fraunhofer Institute for Material and Beam Technology (IWS)  
Winterbergstraße 28, 01277 Dresden, Germany

 Supporting information for this article is available on the WWW under  
<https://doi.org/10.1002/batt.202000286>

 © 2021 The Authors. *Batteries & Supercaps* published by Wiley-VCH GmbH.  
This is an open access article under the terms of the Creative Commons Attribution License, which permits use, distribution and reproduction in any medium, provided the original work is properly cited.

electrolyte.<sup>[18]</sup> Therefore, mostly high electrolyte volumes ( $>10 \mu\text{L mg}_{\text{s}}^{-1}$ ) have been utilized.<sup>[1,4]</sup> However, to realize high energy density prototype cells it is necessary to employ low electrolyte/sulfur (E:S) ratios.<sup>[3,4]</sup> Usually, a low E:S ratio in DME/DOL is accompanied by a decreased cycling performance as the conversion mechanism in this electrolyte needs a certain solvent amount. A fundamental change of the conversion reaction has turned out to be a suitable approach to enable Li–S cell chemistries under lean electrolyte conditions.<sup>[2,8]</sup> Thus, sulfur utilization becomes less dependent on the applied electrolyte volume and consequently, Li–S prototype cells with low E/S ratios can be realized.<sup>[19,20]</sup>

One of the first approaches was reported as “solvent in salt” concept, while high conductive salt concentrations are employed and therefore, the dissolution-based mechanism is transformed into a quasi-solid-state conversion.<sup>[21]</sup> However, a limitation of this concept is the high viscosity of the electrolytes provoked by the high salt concentration. Hence, non-solvating hydrofluorinated ethers (HFE) as “diluent” have been introduced to create sparingly solvating electrolytes.<sup>[22–30]</sup> One promising electrolyte system is the combination of the hydrofluoroether 1,1,2,2-tetrafluoroethyl-2,2,3,3-tetrafluoropropyl ether (TTE) with sulfolane (tetramethylene sulfone, TMS).<sup>[31,32]</sup> Using the TMS/TTE electrolyte stable cycling performance on pouch cell level (3.7 Ah) has been already demonstrated at very low electrolyte amount of  $2.6 \mu\text{L mg}_{\text{s}}^{-1}$ .<sup>[31]</sup>

By developing new electrolyte formulations with reduced LiPS solubility often a standard sulfur cathode containing commercial carbon black or self-developed carbon material is used.<sup>[20,23–31,33]</sup> So far, less is known about the impact of the carbon porosity on the electrochemical performance and active material utilization when the redox reaction is changed into a quasi-solid-state mechanism.

In this study, we analyze the impact of pore architecture for this lean TMS/TTE-electrolyte concept by comparing four porous carbon materials differing in pore architecture as scaffolds in Li–S cathodes. Two commercially available activated carbons and two hierarchical porous carbons are investigated. The latter are obtained by a customized carbothermal reduction process using zinc-based templates.<sup>[34,35]</sup> This class of carbons enables a unique pore

structure with high specific surface areas as well as total pore volumes. By evaluating different cathode materials at low electrolyte amount ( $5 \mu\text{L mg}_{\text{s}}^{-1}$ ), their ability for the sulfur conversion via quasi-solid-to-solid reaction mechanism as well as the potential of generation of a protective solid-electrolyte interface (SEI) on cathode surface is studied. Furthermore, the influence of the carbon porosity on the reaction kinetics of the polysulfide conversion is discussed.

## 2. Results and Discussion

Initially, the different carbon scaffolds were investigated regarding their material properties and afterwards analyzed as Li–S cathodes with the sparingly polysulfide solvating TMS/TTE electrolyte. Hierarchical porous carbons as model carbons with higher pore volume were synthesized by carbothermal reduction process, while pyrolysis and template removal occurs in one step without further purification.<sup>[34,35]</sup> Despite the harsh synthesis conditions during the pyrolysis, highly porous carbons with different defined pore structures are obtained. Moreover, two commercial activated carbons with only micro- or mesopores are further characterized.

### 2.1. Material Characterization

All pristine carbon materials were investigated by  $\text{N}_2$  physisorption at  $-196^\circ\text{C}$ . According to the physisorption data (Figure 1(A)), different isotherms are determined. A type I(b) isotherm regarding the IUPAC classification<sup>[36]</sup> as well as a high specific BET surface area (SSA) of  $1653 \text{ m}^2 \text{ g}^{-1}$  is observed for AC-1. The sample AC-2 exhibits a slightly reduced SSA of  $1554 \text{ m}^2 \text{ g}^{-1}$  and shows a type IV(a) isotherm with a type H4 hysteresis. A mixed type I (micropore regime) and type IV (mesopore regime) isotherm with H3(b) hysteresis and specifically high SSA of  $2717 \text{ m}^2 \text{ g}^{-1}$  is observed for HPC-1 due to an increased gas uptake in the low relative pressure range, reflecting a high micropore volume. In contrast, the sample HPC-2 shows a reduced SSA of  $1745 \text{ m}^2 \text{ g}^{-1}$  and displays a type IV(a) isotherm with a type H3

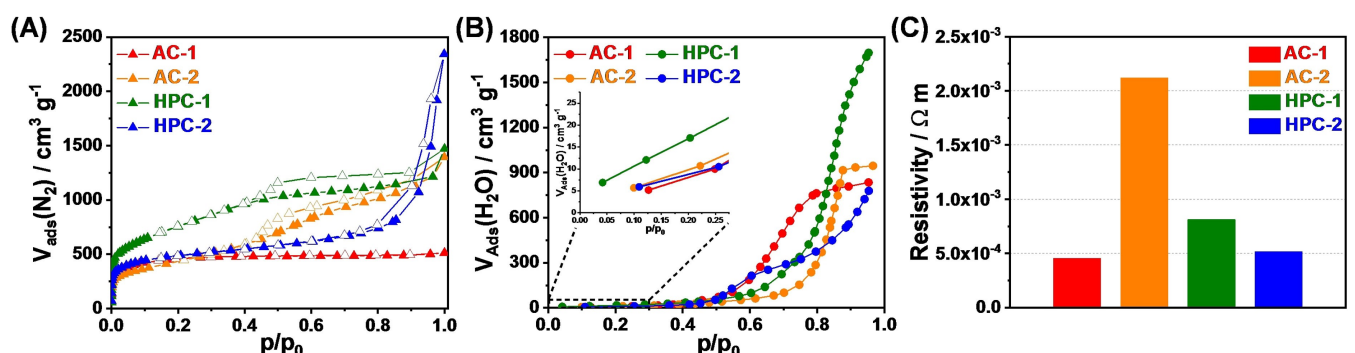


Figure 1. Nitrogen physisorption isotherms at 77 K (A), water adsorption branches at 298 K (B), and the resistivity (C) of the pristine carbon materials.

hysteresis. The isotherm shapes clearly reveal the different pore architectures (Figure S1). Hence, total pore volumes of  $0.83 \text{ cm}^3 \text{ g}^{-1}$ ,  $2.07 \text{ cm}^3 \text{ g}^{-1}$ ,  $2.16 \text{ cm}^3 \text{ g}^{-1}$  and  $3.37 \text{ cm}^3 \text{ g}^{-1}$  are observed for AC-1, AC-2, HPC-1 and HPC-2, respectively. Regarding their pore structures the carbon materials exhibit different amounts of micropores (AC-1: 72%, AC-2: 7%, HPC-1: 24%, HPC-2: 13%). Consequently, different mesopore volume values of  $0.23 \text{ cm}^3 \text{ g}^{-1}$  for AC-1,  $1.92 \text{ cm}^3 \text{ g}^{-1}$  for AC-2,  $1.63 \text{ cm}^3 \text{ g}^{-1}$  for HPC-1 and  $2.95 \text{ cm}^3 \text{ g}^{-1}$  for HPC-2 are determined.

The surface polarity of the carbon scaffolds was characterized by water adsorption measurements (Figure 1(B)). The adsorption branches for all samples show a type V shape according to the IUPAC classification.<sup>[36]</sup> Especially at low relative pressures ( $p/p_0 < 0.4$ ), almost no water uptake is observed. However, at higher  $p/p_0$  values, the volume of adsorbed water or the cluster formation increases, respectively. Moreover, the shapes of the adsorption branches are different due to the porosity properties of the corresponding carbon material. Thus, HPC-1 shows the highest water uptake of  $1697 \text{ cm}^3 \text{ g}^{-1}$  compared to the other samples (AC-1:  $834 \text{ cm}^3 \text{ g}^{-1}$ , AC-2:  $946 \text{ cm}^3 \text{ g}^{-1}$ , HPC-2:  $779 \text{ cm}^3 \text{ g}^{-1}$ ). Additionally, a slight shift to lower relative pressures is observed for the adsorption branch of HPC-1 which indicates a slightly increased hydrophilicity due to the enhanced amount of micropores.

To reveal the impact of the conductivity, pristine carbons were investigated by resistivity measurements. Comparable resistivity values of  $4.60 \times 10^{-4} \Omega \text{ m}$ ,  $8.10 \times 10^{-4} \Omega \text{ m}$ , and  $5.10 \times 10^{-4} \Omega \text{ m}$  are obtained for AC-1, HPC-1 and HPC-2,

respectively. Interestingly, a slightly lower conductivity ( $2.10 \times 10^{-3} \Omega \text{ m}$ ) is determined for the AC-2 scaffold. As the carbon materials are compressed during this experiment the particle size as well the particle morphology affects the resistivity, especially in terms of the compression rate of the material.<sup>[37,38]</sup>

Furthermore, Raman spectroscopy was carried out to analyze the degree of graphitization of the carbon host structures. Raman spectra (Figure S2) display the two specific bands for carbon materials at  $\sim 1342 \text{ cm}^{-1}$  (D-band) and  $\sim 1593 \text{ cm}^{-1}$  (G-band). In this regard, the D-band correlates with the breathing mode of defects or disorder, while the G-band arises from the symmetrical stretching mode of graphitic domains with  $\text{sp}^2$  hybridization.<sup>[39]</sup> The ratio  $I_D/I_G$  can point out differences in graphitization degrees of carbon materials and the length of ordered structures inside the carbon backbone.<sup>[40]</sup> Both HPC samples exhibit comparable  $I_D/I_G$  values of 0.97 (HPC-1) and 1.00 (HPC-2) due to the analogue synthesis route. In contrast, AC-1 shows a slightly higher  $I_D/I_G$  ratio of 1.14, which could possibly indicate more disordered structures or a higher amount of defects. Interestingly, the activated carbon material AC-2 reveals a reduced  $I_D/I_G$  ratio of 0.86 compared to the other samples suggesting probably a higher amount of atoms with  $\text{sp}^2$  hybridization.

To obtain more insights into the particle morphology, all pristine carbon materials were characterized with scanning electron (SEM) and transmission electron (TEM) microscopy. According to the SEM images (Figure 2), a wide distribution of different particle sizes is observed for all samples. AC-1 exhibits sharp-edged particles with a smooth surface and

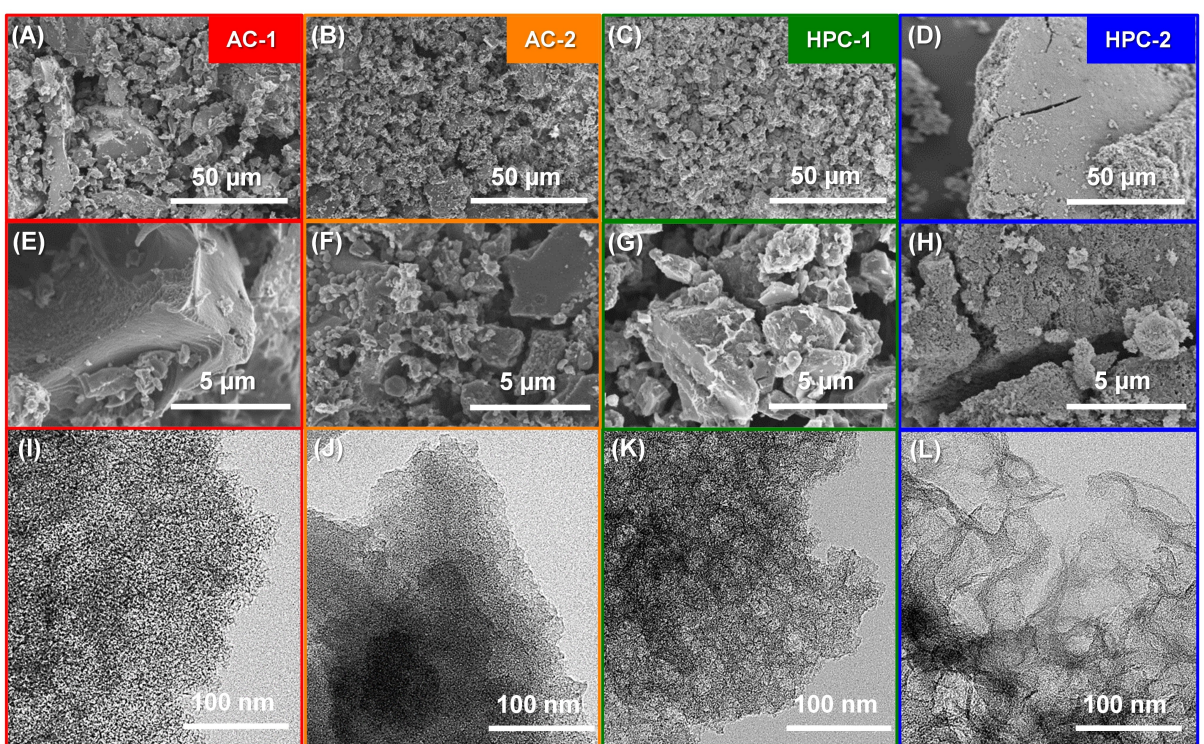


Figure 2. SEM (A–H) and TEM (I–L) images of the pristine carbon materials.

particle sizes up to 50  $\mu\text{m}$ . The TEM image of AC-1 (Figure 2(I)) displays less ordered areas, which confirms the increased  $I_D/I_G$  ratio. In contrast to AC-1, the carbon AC-2 shows a narrow particle size distribution with a higher amount of smaller particles (Figure 2(B,F)) and a slightly enhanced number of ordered structures (Figure 2(J)). This could be the reason for the increased resistivity despite lower  $I_D/I_G$  ratio, since larger particles or aggregate structures provide more pathways for the electrical conductivity due to an enhanced probability of contact between the carbon particles.<sup>[38]</sup> Additionally, a few isolated spherical defects are noticeable at the particle surface of AC-2 (Figure 2(F)) which could possibly contribute to the increased resistivity as well. In contrast to the activated carbons, the particles of both HPC samples show cracks and a rough surface due to the harsh conditions of the carbothermal reduction. However, a similar trend regarding the influence of the particle size on the conductivity is determined for the HPC samples. Hence, HPC-1 shows reduced particle sizes ( $< 10 \mu\text{m}$ ) and thus, a slightly higher resistivity is achieved compared to HPC-2. Furthermore, the TEM images support the nitrogen physisorption data, demonstrating the pores are located in the carbon scaffold and showing the increased total pore volumes or wider pore size distributions, respectively.

## 2.2. Electrochemical Characterization in Coin Cells vs. Li/Li<sup>+</sup>

All carbon materials were analyzed as Li–S cathodes vs. Li/Li<sup>+</sup> by employing TMS/TTE as sparingly solvating electrolyte. The prepared cathodes exhibit different sulfur contents as the carbon materials were loaded with different amounts of sulfur (Figure S3, Table S2) depending on their respective pore volume. However, comparable and reasonable sulfur loadings of approx. 2.60 mg<sub>S</sub> cm<sup>-2</sup> were used for the electrochemical evaluation. In order to ensure realistic test conditions for the galvanostatic testing in coin cells, these experiments were carried out under lean electrolyte conditions (E:S=5).

The galvanostatic cycling performance of all cathode materials by using 1.5 M LiTFSI in TMS/TTE electrolyte at C/10

is presented in Figure 3. As formation process, a reduced C-rate of C/20 is applied for the first discharge to overcome kinetic limitations of the electrolyte.<sup>[30,31,41,42]</sup> Remarkably, high initial discharge capacities of 1600 mAh g<sup>-1</sup>, 1157 mAh g<sup>-1</sup>, 1365 mAh g<sup>-1</sup>, 1141 mAh g<sup>-1</sup> are observed for AC-1, AC-2, HPC-1 and HPC-2, respectively. Due to the reduced current at the first discharge the equilibrium time for precipitation of Li<sub>2</sub>S is enhanced and therefore, the sulfur utilization can be significantly improved.<sup>[31,42,43]</sup> Moreover, a correlation between the micropore volume and the value of the initial discharge capacity is indicated (Figure 3(B)). Above a certain percentage of micropores (~20%), increased initial capacities are determined. In addition, all samples exhibit high CE values over 100% suggesting irreversible capacity loss due to side reactions. It is known that fluorinated ethers possibly decompose at the surface of sulfur infiltrated carbon particles during discharge and could generate a solid electrolyte interface (SEI) passivation layer on cathode side.<sup>[26,27,44]</sup> Moreover, carbon properties e.g. particle morphology or defect sites seem to have an effect on the cathodic SEI (CEI) formation. However, with higher initial capacity values the degradation is even higher in the following cycles, especially for AC-1 carbon (2<sup>nd</sup> cycle: 886 mAh g<sup>-1</sup>). Consequently, after five cycles reduced discharge capacities of 836 mAh g<sup>-1</sup> (98.7% CE), 950 mAh g<sup>-1</sup> (98.5% CE), 1073 mAh g<sup>-1</sup> (98.1% CE), 1006 mAh g<sup>-1</sup> (98.8% CE) are observed for AC-1, AC-2, HPC-1 and HPC-2, respectively. Interestingly, a different capacity retention behavior is achieved for further cycles. The cathodes AC-1, AC2 and HPC-2 show almost linear capacity degradation and thus, low capacity values of 204 mAh g<sup>-1</sup> (AC-1), 420 mAh g<sup>-1</sup> (AC-2), 304 mAh g<sup>-1</sup> (HPC-2) are observed after 100 cycles. As the carbons AC-2 and HPC-2 show a reduced amount of micropores the major impact on the sulfur conversion arises from the mesopores. The enhanced capacity degradation of AC-1 is attributed to the reaction in the first cycle, while the high micropores content seems to play a crucial role. Presumably, the increased  $I_D/I_G$  ratio of the AC-1 sample has also a negative impact on the enhanced capacity degradation during cycling. Consequently, AC-2 shows an improved capacity retention compared to HPC-2 due to the slightly increased

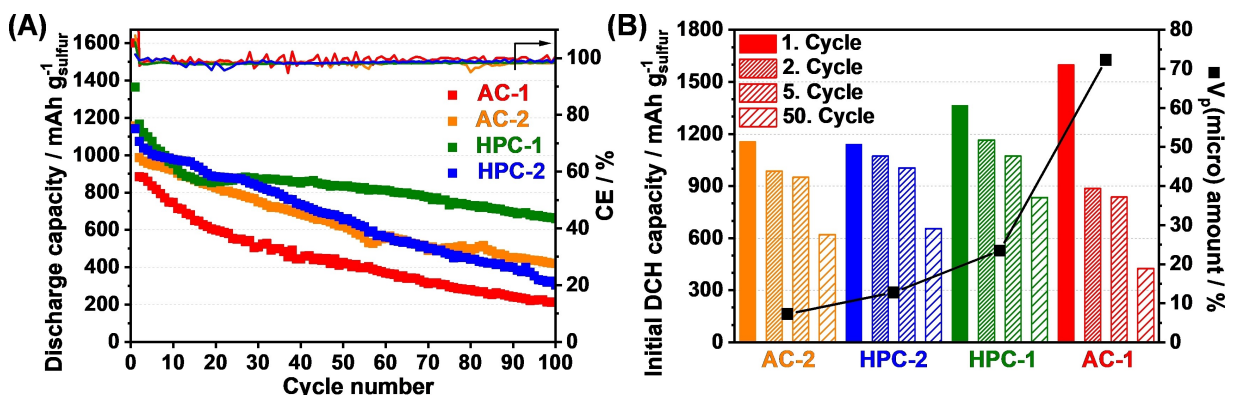
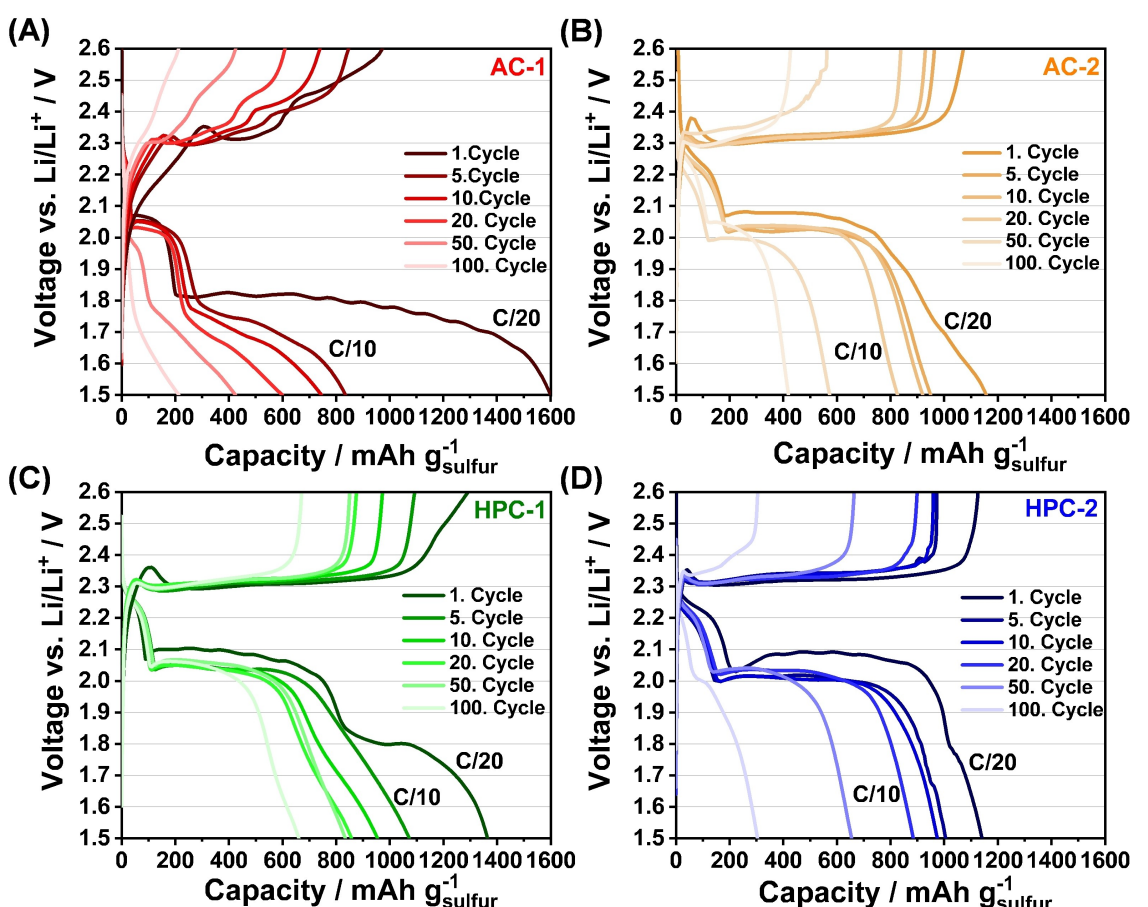


Figure 3. (A) Galvanostatic cycling performances of all samples, (B) correlation of discharge capacities and the percentage amount of the micropore volume.

graphitization degree. Moreover, the conductivity of the pristine carbons and the corresponding electrodes has also an influence on the sulfur utilization. In contrast, an enhanced cycle performance as well as capacity retention is revealed for the HPC-1 scaffold. The porosity properties of HPC-1, especially the high SSA, lead to an enhanced number of active sites for the electron transfer from the conductive carbon to the sulfur species resulting in an improved capacity retention and cycling performance.<sup>[9,35]</sup> In this regard, the SSA values influence the cycle stability as well as sulfur utilization: For HPC-1 with the highest SSA ( $2717 \text{ m}^2 \text{ g}^{-1}$ ), a decent sulfur utilization in the first cycle ( $1365 \text{ mAh g}^{-1}$ ) and highest capacity retention ( $100^{\text{th}}$  cycle:  $661 \text{ mAh g}^{-1}$ ) is observed. Principally, the other three carbons have SSA values in almost the same range ( $1554\text{--}1745 \text{ m}^2 \text{ g}^{-1}$ ). Hence, comparable active material utilizations are determined for HPC-2 and AC-2. The AC-1 carbon in particular has a reduced graphitization degree and possibly undergoes a coating by the described CEI. Consequently, the capacity retention of AC-1 is lower compared to AC-2 and HPC-2. Moreover, the HPC-1 host structure shows an enhanced polarity (Figure 1(B)) which can possibly improve the wettability or the interaction with polar polysulfide

intermediates. Additionally, the enhanced conductivity of HPC-1 appears to have a positive effect on the electrochemical performance as well.

In the corresponding voltage profiles (Figure 4), a remarkable difference between the conductive scaffolds is observed. The sample AC-1 shows the two distinctive discharge plateaus at 2.27 V and 2.07 V according to the formation of long-chain polysulfide intermediates ( $\text{Li}_2\text{PS}_{6-8}$ ) and the transformation of short-chain LiPs.<sup>[15,45]</sup> However, these plateaus, especially the first plateau (2.27 V) are slightly depressed and a significant over-potential is determined due to the suppressed polysulfide solubility as well as high viscosity of the TMS/TTE electrolyte.<sup>[31,46]</sup> Interestingly, an additional third discharge plateau at 1.80 V and a completely different charging behavior is revealed for AC-1, the one with the highest micropore content. By using highly fluorinated ethers the additional discharge plateau is associated to the formation of a protective SEI layer on cathode side as so-called cathode electrolyte interface (CEI), while a reductive decomposition of the ether molecules takes place at the carbon particle surface.<sup>[26,44]</sup> Probably, active material could be encapsulated inside the micropores after the formation of a closed CEI layer on top of the pore entrance. Therefore, a



**Figure 4.** Voltage profiles of the galvanostatic cycling at C/10 of all cathode materials. As formation process, a reduced C-rate of C/20 is applied for the first discharge.

remarkable over-potential is observed for the charging process, particularly for the first charging dip due to hindered Li<sup>+</sup> ion diffusion through the protective CEI layer.<sup>[47]</sup> As a consequence, a reduced active material utilization arises resulting the capacity degradation. Moreover, the first two discharge plateaus extend in the following cycles due to the increasing TMS volume or improved facility of polysulfide solubility.<sup>[31,48]</sup> However, the AC-1 cathode shows the third discharge plateau in further cycles as well and hence, this effect is attributed to conversion of short chain polysulfides (Li<sub>2</sub>S<sub>x</sub>, x=2–4) via quasi-solid-state mechanism being further discussed in the cyclic voltamograms (Figure 5).<sup>[20,49–51]</sup> The quasi-solid-to-solid conversion is mostly reported by applying microporous carbons with confined sulfur as Li–S cathodes in carbonate-based electrolytes.<sup>[47,52]</sup> However, by using electrolyte concepts with restricted LiPS solubility the modified reaction mechanism has also been reported.<sup>[20,25,49]</sup> Consequently, a combination of the commonly solid-liquid-solid and quasi-solid-to-solid conversion is realized with the microporous AC-1 cathode material and the TMS/TTE electrolyte.<sup>[25,53]</sup> Since HPC-1 exhibits also a high amount of micropores, this cathode material shows also the extra plateau at 1.80 V for the first discharge (Figure 4(C)). How-

ever, the first charging and the further voltage slopes are remarkably different compared to AC-1. For the first charging process, a reduced over-potential is achieved and the voltage slope is more comparable to the common solid-liquid-solid reaction mechanism.<sup>[15,45]</sup> The major fraction of the melt-infiltrated sulfur should be available inside the mesopores (75 % of porosity) and thus, only a partial CEI formation could take place on the particle surface. Presumably, a closed CEI layer is not created on top of the mesopores due to the wider distances of the pore walls as already studied for carbonate based materials.<sup>[47]</sup> Hence, the active material cannot be encapsulated or is utilizable for further reactions. Additionally, HPC-1 shows a lower amount of defect sites compared to AC-1 (Table 1) which supports the reduced CEI formation theory. Subsequently, only the two discharge plateaus at 2.25 V and 2.06 V as well as a slightly increasing over-potential are observed in the following cycles for the HPC-1 cathode. In contrast to the microporous carbons, AC-2 and HPC-2 (Figure 4(B,D)) show only two characteristic discharge plateaus (2.25 V and 2.04 V) regard to the formation of long-chain polysulfides (Li<sub>2</sub>PS<sub>6–8</sub>) and the transformation of short-chain LiPS to Li<sub>2</sub>S.<sup>[15,45]</sup> Hence, these scaffolds reveal no additional discharge plateau and a

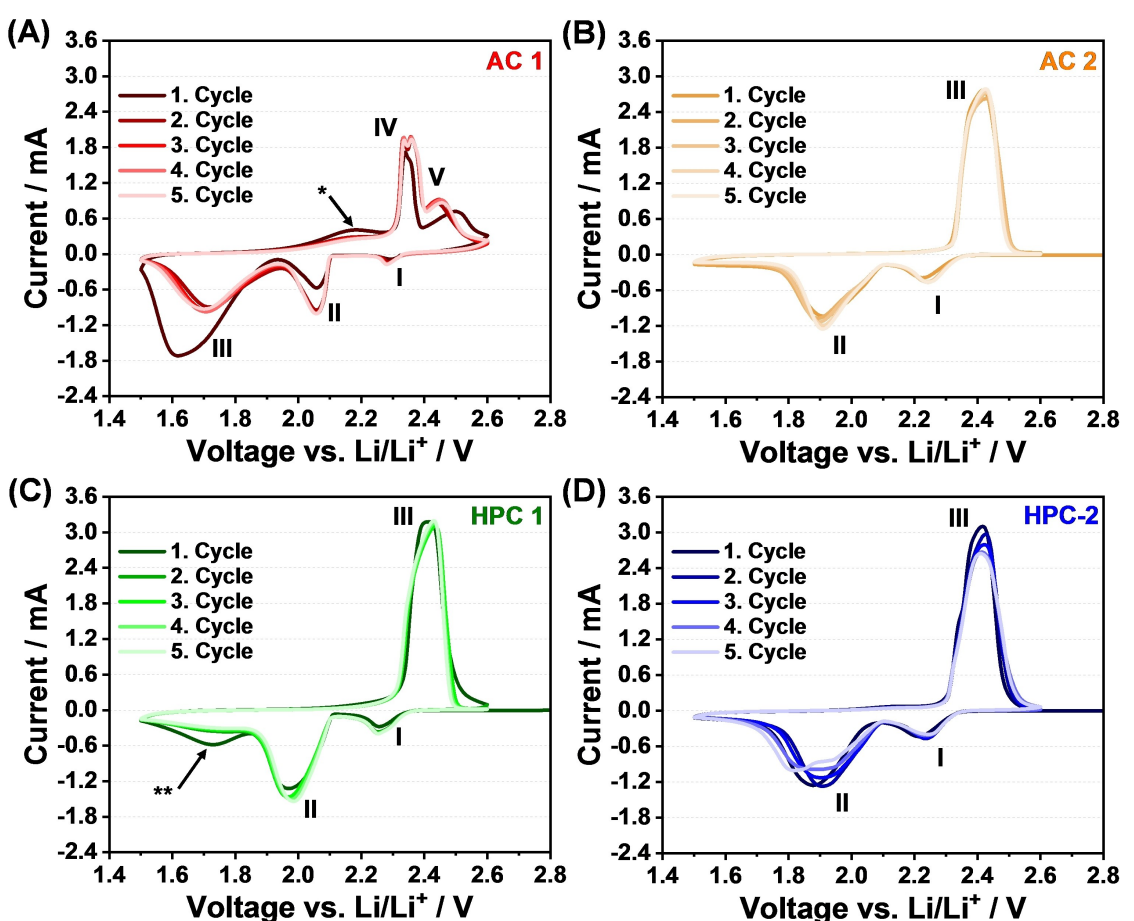


Figure 5. CV curves of all carbon materials as Li–S cathodes at a scan rate of 35  $\mu\text{Vs}^{-1}$  (corresponds to a C-rate of approx. C/20).

**Table 1.** Summary of the structural characterization data: Physisorption data derived from nitrogen isotherms measured at 77 K. Raman spectroscopy data determined using a  $\lambda_{\text{excitation}} = 514 \text{ nm}$ . Resistivity of carbon powders analyzed at  $p = 2 \text{ t}$ .

Sample	$\text{SSA}_{\text{BET}}^{[a]}$ [ $\text{m}^2 \text{g}^{-1}$ ]	$V_p(\text{tot})^{[b]}$ [ $\text{cm}^3 \text{g}^{-1}$ ]	$V_p(\text{micro})^{[c]}$ [ $\text{cm}^3 \text{g}^{-1}$ ]	$V_p(\text{meso})^{[d]}$ [ $\text{cm}^3 \text{g}^{-1}$ ]	$I_b/I_G^{[e]}$	$\rho^{[f]}$ [ $\Omega \text{ m}$ ]
AC-1	1653	0.83	0.60	0.23	1.14	$4.60 \times 10^{-4}$
AC-2	1554	2.07	0.15	1.92	0.86	$2.10 \times 10^{-3}$
HPC-1	2717	2.16	0.53	1.63	0.97	$8.10 \times 10^{-4}$
HPC-2	1745	3.37	0.42	2.95	1.00	$5.10 \times 10^{-4}$

[a] SSA calculated by using Multipoint BET method  $0.05 \leq p/p_0 \leq 0.20$ . [b] Total pore volume was determined at  $p/p_0 = 0.99$ . [c] Micropore volume was calculated by using cumulative pore volume determined by QSDFT (slit, cylindrical pores; adsorption branch) for pores  $< 2 \text{ nm}$ . [d] Mesopore volume was calculated by subtracting micropore volume from total pore volume:  $V_p(\text{meso}) = V_p(\text{tot}) - V_p(\text{micro})$ . [e] Intensities of corresponding band were calculated with a Lorentzian fit (details see experimental section). [f] Powder resistivity was determined by measuring the electrical resistivity under pressure (details see experimental section).

closed CEI layer is not generated. However, a partial CEI formation through the TTE decomposition cannot be excluded as both samples reveal minor modifications at 1.75–1.80 V for the first discharge slope as well as slight overpotential at charging. In addition, for both samples, an increasing over-potential for the second discharge plateau (AC-2: 2.04 V, HPC: 2.02 V) is observed due to the increasing polarization effects during cycling.<sup>[31,44,49]</sup>

To elucidate the altered conversion mechanism and the effect of the third discharge plateau, all cathodes were analyzed by using cyclic voltammetry with a low scan rate of  $15 \mu\text{Vs}^{-1}$  (corresponds to a C-rate of approx. C/20). In Figure 5(A) three reduction peaks at 2.28 V (I), 2.06 V (II), 1.70 V (III) and two oxidation signals at 2.35 V (IV), 2.45 V (V) are observed for the AC-1 sample. Especially, the broad peak at 1.61 V in the first scan reveals the irreversible TTE decomposition or CEI generation on the carbon surface.<sup>[26,27,44]</sup> In further cycles, the AC-1 cathode shows the combination of the conversion mechanism as well.<sup>[28,30,33]</sup> In the anodic scan, an additional shoulder at 2.18 V (\*) is achieved which could attribute to the solid transformation of  $\text{Li}_2\text{S}$  to low order PS.<sup>[54]</sup> Hence, with the help of a mostly microporous scaffold the quasi-solid-state conversion is demonstrated by using TMS/TTE electrolyte. In contrast to AC-1, only a single reduction peak at 1.72 V (\*\*) is observed in the first scan for the HPC-1 cathode. Additionally, a broad oxidation signal at 2.42 V (III) is detected for AC-2, HPC-1 and HPC-2, which displays a slightly altered reaction mechanism, compared to AC-1. The following CV curves of AC-2 and HPC-2 are more comparable to the regular solid-liquid-solid transformation.<sup>[15]</sup> Therefore, two reduction peaks at  $\sim 2.23 \text{ V}$  (I) and  $\sim 1.90 \text{ V}$  (II) are observed for the AC-2 and HPC-2. Both materials show an increasing over-potential with higher cycle number regard to polarization effects which probably arise due to the lower number of active sites for the electron transfer to the intermediates. Summarizing, the porosity of the sulfur host structure has an important influence on the conversion, electrolyte depletion, and CEI formation mechanism by employing TMS/TTE electrolyte.

To obtain more insights into kinetics and thermodynamics of the changed conversion mechanism during the discharge process, all cathodes were analyzed by means of galvanostatic intermittent titration technique (GITT).<sup>[55]</sup> For

these experiments the sulfur electrodes are analyzed in coin cells versus a lithium metal anode at room temperature. As formation process, the cells were discharged at C/20 and charged at C/10. Afterwards, the open circuit potential (OCP) is monitored during the discharge for 2 h equilibrium time. The equilibrium voltage is plotted versus the discharge capacity (Figure 6). While employing a constant current and detecting the corresponding OCP during the discharge, kinetically limiting processes of polysulfide conversion are investigated.<sup>[20,49]</sup>

Generally, the constant current voltage response proceeds in good accordance with the galvanostatic cycling results (Figure 4) for all cathode materials. When discharging the cells under GITT conditions the difference between OCP and the constant current gradually increases with rising depth of discharge. However, the typical voltage knee between the distinctive plateaus of the OCP measurement is shifted to lower discharge capacities ( $\sim 200 \text{ mAh g}^{-1}$ ) compared to previous studies with sparingly polysulfide solvating electrolytes.<sup>[20,29,49]</sup> Thus, the formation of long-chain polysulfides is substantially reduced in the TMS/TTE electrolyte.<sup>[31]</sup>

For the four employed carbon scaffolds, a remarkable difference in GITT voltage profiles is observed. As before, the sample AC-1 shows only a reduced first discharge plateau and the voltage of the first constant current step drops to value of 2.03 V (I\*). This low first stage voltage indicates an earlier transformation of low-order LiPS since higher voltages corresponds to long-chain polysulfide intermediates.<sup>[49]</sup> Moreover, the first OCP point is determined at the equilibrium state for the commonly second discharge plateau at 2.20 V. This phenomenon is described as direct conversion of solid sulfur ( $\text{S}_8$ ) to  $\text{Li}_2\text{S}_4$  via quasi-solid-solid reaction.<sup>[29,49]</sup> It is known from glyme-based electrolyte system that the intermediate  $\text{Li}_2\text{S}_3$  can be generated which acts as redox mediator and undergoes disproportionation as well as synproportionation reactions.<sup>[49]</sup> This proposal can be transferred to the TMS/TTE electrolyte as restricted polysulfide solubility is also achieved.<sup>[31]</sup> Thus, insulating products  $\text{S}_8$  and  $\text{Li}_2\text{S}$  can be (re)activated and utilized in the following reaction cascade.<sup>[20,49]</sup> However, the GITT experiment of AC-1 differs compared to previous studies with reference cathodes as with increasing constant current steps a nearly consistent relaxation (II\* in

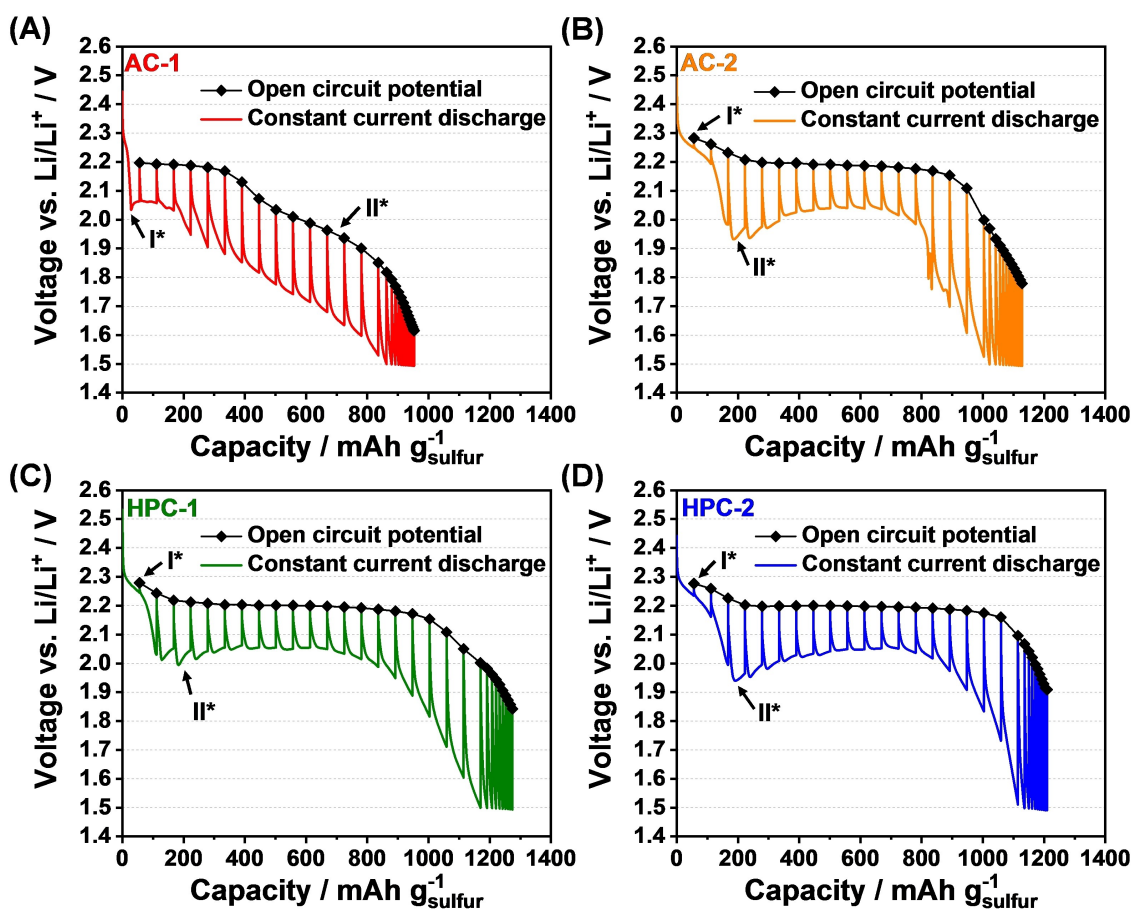


**Figure 6.** GITT voltage profiles and open circuit potentials of the corresponding carbon host material measured with 20 min discharge at C/10 followed by 2 h pause.

Figure 6(A)) rate is observed after the second plateau.<sup>[26,29,49,51]</sup> The uniform reduction of the reaction kinetics can be attributed to the hindered Li<sup>+</sup> ion diffusion through the CEI layer or reduced Li<sub>2</sub>S precipitation.<sup>[47]</sup> Hence, larger Li<sub>2</sub>S particles could be generated and the enhanced precipitation terminates the discharge process. The Li<sub>2</sub>S agglomeration induces the observed over-potential during charging as well as the linear capacity fading as smaller Li<sub>2</sub>S particles can be better oxidized or transformed into LiPS intermediates.<sup>[56]</sup> It seems that the microporous cathode material favors the quasi-solid state transformation of the confined short-chain LiPS inside the pores. In contrast, the other carbon scaffold materials AC-2, HPC-1, and HPC-2 show the first OCP point at the first discharge plateau at ~2.28 V (I\*). Consequently, with larger pore sizes a higher proportion of high order polysulfides can be assumed for the participation in the sulfur conversion mechanism. Therefore, the corresponding voltage knees are more pronounced, especially for AC-2 and HPC-2 (Figure 6(B,D)) due to the viscosity increase regarding the cluster formation of low-order LiPS.<sup>[57]</sup> However, a combined reaction mechanism (solid-liquid-solid and quasi-solid-solid) is still suggested due to low polysulfide solubility.<sup>[31]</sup> At the end of discharge, large amounts of Li<sub>2</sub>S

accumulate and the relaxation rate increases due to the reduced charge-transfer from the carbon host structure to the active material.<sup>[20,31]</sup> Finally, the increasing Li<sub>2</sub>S agglomeration or precipitation terminates the discharge process. These findings give evidence that the carbon porosity impacts the reaction kinetics of the polysulfide conversion by using TMS/TTE as sparingly polysulfide solvating electrolyte.

### 3. Conclusions

Four carbon materials with different pore structures and varying pore volume were studied as sulfur model cathodes in operation with TMS/TTE electrolyte to understand the impact of the scaffold porosity (micropores, mesopores and hierarchical pores) on the modified conversion mechanism of sparingly polysulfide solvating electrolytes. For the four carbon materials, differences in particle morphology, graphitization degree and conductivity were elaborated and discussed. Galvanostatic cycling performances at low electrolyte volume (E:S=5) revealed stable cycling up to 100 cycles for all cathodes. The microporous electrodes showed an

additional third discharge plateau, which displays the quasi-solid-to-solid mechanism and has not been shown for TMS/TTE electrolytes before. CV experiments indicated the generation of a SEI layer on the cathode originating from the decomposition of the TTE solvent. The cathodic SEI formation is more pronounced in microporous cathode materials, which can be attributed to the smaller pore entrance and dangling bonds due to the more disordered structure. When a closed CEI layer can be generated the active material should be trapped inside the micropores resulting in a more polarized quasi-solid-state sulfur conversion. For the three other investigated porous carbon materials a mix-type sulfur conversion cannot be excluded whereas the common solid-liquid-solid reaction mechanism is more observed. GITT measurements underlined the assumption that the porosity of the conductive scaffolds influence the kinetic regimes of the conversion of polysulfide intermediates by using TMS/TTE electrolyte. These results provide a new mechanistic view on the operation of Li–S batteries with sparingly solvating electrolytes. The adaption of the porous carbon cathode structure is essential to achieve high, especially volumetric, energy densities for the exploration of new electrolyte systems.

## Experimental Section

### Carbon materials

Hierarchical porous carbons (HPC) were prepared using a carbothermal reduction process as reported elsewhere.<sup>[34,35]</sup> Zinc citrate dihydrate (Alfa Aesar, reagent grade) or zinc oxide nanoparticles (US Research Nanomaterials Inc., product specification 10–30 nm) were used as templates to produce HPC-1 or HPC-2, respectively. The carbothermal reduction was carried out in a horizontal tubular furnace ( $\varnothing$ : 50 mm) under argon flow (0.60 slm) by a heating rate of  $5^{\circ}\text{C min}^{-1}$  to 950 °C for 2 h. Additionally, two commercially available activated carbons, AC-1 (Cabot Norit Nederland B.V) and AC-2 (GTD Graphit Technologie GmbH) were investigated.

### Electrode preparation

Li–S cathodes were prepared using a manual solvent-free roll process reported elsewhere.<sup>[58]</sup> Prior to sulfur infiltration, all carbon materials were dried. The microporous carbon (AC-1) was activated at 200 °C for 12 h under vacuum. The other samples were dried at 120 °C overnight. Different amounts of pristine sulfur (Carl Roth, 99.5%) were mixed with the corresponding scaffold depending to their pore volumes. The melt-infiltration process was carried out at 155 °C for 30 min under ambient conditions. The as-prepared C/S composites were mixed with multi-walled carbon nanotubes (MWCNT, Nanocyl 7000) as conductive additive and poly (tetrafluoroethylene) (PTFE) as binder in a weight ratio of 85:12:3. After homogenization and intensive grinding, electrode sheets were prepared using shearing forces. Subsequently, the free-standing cathode films were laminated on a primer coated aluminum current collector for electrochemical characterization. For coin cell testing circular electrodes with a diameter of 15 mm (varying thickness: 100 ±

20  $\mu\text{m}$ ) were punched out with active material loadings of  $2.60 \pm 0.30 \text{ mg s cm}^{-2}$  and electrode densities of  $0.56 \pm 0.10 \text{ cm}^3 \text{ g}^{-1}$ .

### Structural characterization

Nitrogen physisorption measurements at  $-196^{\circ}\text{C}$  (77 K) were performed on a Rubotherm BELSORP after degassing the samples for 12 h at 200 °C under vacuum. Specific surface areas were calculated based on multi-point Brunauer-Emmett-Teller (BET) method in the range of 0.05–0.20  $\text{p/p}_0$ . The total pore volumes were determined at a relative pressure  $\text{p/p}_0$  of 0.99. Micropore volumes were calculated from the cumulative pore volumes at a diameter of 2 nm using the Quenched-Solid-Density-Theory (QSDFT) method for carbon materials (slit/cylindrical pores, adsorption branch). Water adsorption measurements were carried out on a Rubotherm BELSORB at 25 °C (298 K) after as mentioned degassing conditions.

The thermal analysis was conducted with a Netzsch STA 409 PC LUXX with a heating rate of  $5 \text{ K min}^{-1}$  under synthetic air conditions.

Raman spectroscopy data were collected using a Renishaw *inVia* Raman spectrometer under ambient conditions and a laser excitation wavelength of 514 nm. By determining the ratio of the peak intensities  $I_D/I_G$ , the intensities of the D- and the G-band were calculated by fitting the spectra with a Lorentzian function for each band using OriginLab® 2019.

Specific resistivity or conductivity was determined for a carbon pellet (diameter: 1 cm) after compression in a hollow cylinder using a punch press (max.  $p = 2 \text{ t}$ ) in a customized set-up. The punch as well as the bottom of the cylinder are the measurement electrodes. The electric resistivity was determined during the compression process between these two electrodes. The specific resistivity of the carbon materials was derived from the measured resistivity at  $p = 2 \text{ t}$ , the area, and the thickness of the pellet.

The morphology of carbon materials was characterized by Scanning Electron Microscopy (SEM) on a SU8020 (Hitachi) with a triple detector system for secondary and low-energy back-scattered electrons operating with an acceleration voltage of 2 kV. Prior to measurement, the samples were fixed on a carbon pad. Transmission electron microscopy (TEM) was carried out in a JEOL JEM 1400plus using a LaB<sub>6</sub> cathode with an acceleration voltage of 120 kV. The samples were dispersed in isopropanol, dropped on a copper grid and dried overnight before measuring.

### Coin cell assembly and electrochemical characterization

Electrolyte preparation as well as cell assembly was performed in an argon-filled glove box (MBraun, conditions:  $< 0.10 \text{ ppm O}_2$  and  $\text{H}_2\text{O}$ ). The conductive salt lithium bis(trifluoromethanesulfonyl)imide (LiTFSI, Gotion Inc.) was dissolved in tetramethylene sulfone (TMS, Kishida Chemical Co., Ltd.) and 1,1,2,2-tetrafluoroethyl-2,2,3,3-tetrafluoropropyl ether (TTE, Daikin Chemical Europe GmbH), 1:1 by volume and stirred overnight.<sup>[31]</sup>

For electrochemical characterization, CR2016 coin cells (MTI Corp.) were assembled by stacking the corresponding C/S cathode, a PE separator (diameter: 19 mm, thickness: 12  $\mu\text{m}$ ), an elemental lithium chip (MTI Corp., diameter: 16.5 mm, thickness: 250  $\mu\text{m}$ , purity: 99.9%) and a stainless steel spacer (Fraunhofer IWS, diameter: 16.3 mm, thickness: 1000  $\mu\text{m}$ ). The C/S cathodes

were dried under vacuum at 50 °C for 1 h prior to cell assembly. Before sealing, a defined amount of 5  $\mu\text{L mg}_\text{s}^{-1}$  of 1.5 M LiTFSI in TMS/TTE (v/v = 1/1) electrolyte was added. For cyclic voltammetry experiments, a fixed electrolyte volume of 30  $\mu\text{L}$  (approx. 6  $\mu\text{L mg}_\text{s}^{-1}$ ) of TMS/TTE electrolyte was used.

All electrochemical measurements were performed at constant laboratory temperature ( $22 \pm 2^\circ\text{C}$ ). The capacity and long-term stability of the cells were characterized by galvanostatic cycling with a battery tester CTS-Lab (BaSyTec). The coin cells were cycled between 1.50–2.60 V vs. Li/Li<sup>+</sup>. As formation process, a current rate of C/20 for the first discharge was used, and subsequently, cycling was conducted at C/10 (1 C = 1672 mAh g<sub>s</sub><sup>-1</sup>). The Coulombic efficiency (CE) was determined by dividing the discharge (lithiation) capacity by the charge (delithiation) capacity. Cyclic voltammograms were measured using a VSP-300 multichannel potentiostat/galvanostat (Bio-Logic). Scans were performed in a voltage range of 1.50–2.60 V vs. Li/Li<sup>+</sup> with a scan rate of 15  $\mu\text{V s}^{-1}$  (corresponding to a C-rate of approx. C/20).

## Acknowledgements

This work has received funding from the European Union's Horizon 2020 research and innovation program through the project "LiSA" (GA No. 814471). Open access funding enabled and organized by Projekt DEAL.

## Conflict of Interests

The authors declare no conflicts of interests.

**Keywords:** lithium–sulfur battery • cathode materials • carbon porosity variation • sparingly solvating electrolyte • mechanistic insights

- [1] J. Lochala, D. Liu, B. Wu, C. Robinson, J. Xiao, *ACS Appl. Mater. Interfaces* **2017**, *9*, 24407.
- [2] S.-H. Chung, C.-H. Chang, A. Manthiram, *Adv. Funct. Mater.* **2018**, *28*, 1801188.
- [3] S. Dörfler, H. Althues, P. Härtel, T. Abendroth, B. Schumm, S. Kaskel, *Joule* **2020**, *4*, 539.
- [4] T. Cleaver, P. Kovacic, M. Marinescu, T. Zhang, G. Offer, *J. Electrochem. Soc.* **2018**, *165*, A6029–A6033.
- [5] a) X.-B. Cheng, R. Zhang, C.-Z. Zhao, Q. Zhang, *Chem. Rev.* **2017**, *117*, 10403; b) S. Chen, C. Niu, H. Lee, Q. Li, L. Yu, W. Xu, J.-G. Zhang, E. J. Dufek, M. S. Whittingham, S. Meng, *Joule* **2019**, *3*, 1094.
- [6] S. S. Zhang, *J. Power Sources* **2013**, *231*, 153.
- [7] J. Yan, X. Liu, B. Li, *Adv. Sci.* **2016**, *3*, 1600101.
- [8] G. Li, S. Wang, Y. Zhang, M. Li, Z. Chen, J. Lu, *Adv. Mater.* **2018**, *30*, e1705590.
- [9] S. Dörfler, P. Strubel, T. Jaumann, E. Troschke, F. Hippauf, C. Kensy, A. Schökel, H. Althues, L. Giebel, S. Oswald, *Nano Energy* **2018**, *54*, 116.
- [10] a) C. Schneidermann, C. Kensy, P. Otto, S. Oswald, L. Giebel, D. Leistenschneider, S. Grätz, S. Dörfler, S. Kaskel, L. Borchardt, *ChemSusChem* **2019**, *12*, 310; b) C. Kensy, P. Härtel, J. Maschita, S. Dörfler, B. Schumm, T. Abendroth, H. Althues, B. V. Lotsch, S. Kaskel, *Carbon* **2020**, *161*, 190; c) E. Troschke, C. Kensy, F. Haase, S. Dörfler, Y. Joseph, B. V. Lotsch, S. Kaskel, *Batteries & Supercaps* **2020**, *3*, 1069.
- [11] a) I. Bauer, S. Thieme, J. Brückner, H. Althues, S. Kaskel, *J. Power Sources* **2014**, *251*, 417; b) R. Bugga, J.-P. Jones, S. C. Jones, F. C. Krause, J. Pasalic, D. S. Ganapathi, M. Hendrickson, E. J. Plichta, *J. Electrochem. Soc.* **2018**, *165*, A6021–A6028; c) J. He, Y. Chen, A. Manthiram, *Energy Environ. Sci.* **2018**, *11*, 2560.
- [12] a) X. Liang, Q. Pang, I. R. Kochetkov, M. S. Sempere, H. Huang, X. Sun, L. F. Nazar, *Nat. Energy* **2017**, *2*, 652; b) Y. Liu, D. Lin, P. Yuen, K. Liu, J. Xie, R. H. Dauskardt, Y. Cui, *Adv. Mater.* **2017**, *29*; c) M. Baloch, D. Shanmukaraj, O. Bondarchuk, E. Bekaert, T. Rojo, M. Armand, *Energy Storage Mater.* **2017**, *9*, 141; d) Y. Xu, L. Wang, W. Jia, Y. Yu, R. Zhang, T. Li, X. Fu, X. Niu, J. Li, Y. Kang, *Electrochim. Acta* **2019**, *301*, 251.
- [13] S. Dörfler, S. Walus, J. Locke, A. Fotouhi, D. J. Auger, N. Shateri, T. Abendroth, P. Härtel, H. Althues, S. Kaskel, *Energy Technol.* **2020**.
- [14] M. Barghamadi, A. S. Best, A. I. Bhatt, A. F. Hollenkamp, M. Musameh, R. J. Rees, T. Rüther, *Energy Environ. Sci.* **2014**, *7*, 3902.
- [15] M. Wild, L. O'Neill, T. Zhang, R. Purkayastha, G. Minton, M. Marinescu, G. J. Offer, *Energy Environ. Sci.* **2015**, *8*, 3477.
- [16] a) S. S. Zhang, *Electrochim. Acta* **2012**, *70*, 344; b) S. Xiong, K. Xie, Y. Diao, X. Hong, *J. Power Sources* **2014**, *246*, 840; c) S. S. Zhang, *J. Power Sources* **2016**, *322*, 99; d) B. D. Adams, E. V. Carino, J. G. Connell, K. S. Han, R. Cao, J. Chen, J. Zheng, Q. Li, K. T. Mueller, W. A. Henderson, *Nano Energy* **2017**, *40*, 607.
- [17] H. Schneider, T. Weiß, C. Scordilis-Kelley, J. Maeyer, K. Leitner, H.-J. Peng, R. Schmidt, J. Tomforde, *Electrochim. Acta* **2017**, *243*, 26.
- [18] a) J. Brückner, S. Thieme, H. T. Grossmann, S. Dörfler, H. Althues, S. Kaskel, *J. Power Sources* **2014**, *268*, 82; b) S. Thieme, J. Brückner, A. Meier, I. Bauer, K. Gruber, J. Kaspar, A. Helmer, H. Althues, M. Schmuck, S. Kaskel, *J. Mater. Chem. A* **2015**, *3*, 3808.
- [19] a) M. Hagen, D. Hanselmann, K. Ahlbrecht, R. Maça, D. Gerber, J. Tübke, *Adv. Energy Mater.* **2015**, *5*, 1401986; b) L. Cheng, L. A. Curtiss, K. R. Zavadil, A. A. Gewirth, Y. Shao, K. G. Gallagher, *ACS Energy Lett.* **2016**, *1*, 503.
- [20] C. Weller, J. Pampel, S. Dörfler, H. Althues, S. Kaskel, *Energy Technol.* **2019**, *7*, 1900625.
- [21] a) E. S. Shin, K. Kim, S. H. Oh, W. I. Cho, *Chem. Commun.* **2013**, *49*, 2004; b) L. Suo, Y.-S. Hu, H. Li, M. Armand, L. Chen, *Nat. Commun.* **2013**, *4*, 1481; c) K. Dokko, N. Tachikawa, K. Yamauchi, M. Tsuchiya, A. Yamazaki, E. Takashima, J.-W. Park, K. Ueno, S. Seki, N. Serizawa, *J. Electrochem. Soc.* **2013**, *160*, A1304–A1310; d) C. Qu, Y. Chen, X. Yang, H. Zhang, X. Li, H. Zhang, *Nano Energy* **2017**, *39*, 262; e) D. Shanmukaraj, S. Lois, S. Fantini, F. Malbosc, M. Armand, *Chem. Mater.* **2018**, *30*, 246; f) Y. Yamada, J. Wang, S. Ko, E. Watanabe, A. Yamada, *Nat. Energy* **2019**, *4*, 269.
- [22] S. Drvarić Talian, S. Jeschke, A. Vizintin, K. Pirnat, I. Arčon, G. Aquilanti, P. Johansson, R. Dominko, *Chem. Mater.* **2017**, *29*, 10037.
- [23] H. Lu, Y. Yuan, K. Zhang, F. Qin, Y. Lai, Y. Liu, *J. Electrochem. Soc.* **2015**, *162*, A1460–A1465.
- [24] C. Zu, N. Azimi, Z. Zhang, A. Manthiram, *J. Mater. Chem. A* **2015**, *3*, 14864.
- [25] S. Gu, R. Qian, J. Jin, Q. Wang, J. Guo, S. Zhang, S. Zhuo, Z. Wen, *Phys. Chem. Chem. Phys.* **2016**, *18*, 29293.
- [26] J. Zheng, G. Ji, X. Fan, J. Chen, Q. Li, H. Wang, Y. Yang, K. C. DeMella, S. R. Raghavan, C. Wang, *Adv. Energy Mater.* **2019**, *9*, 1803774.
- [27] N. Azimi, W. Weng, C. Takoudis, Z. Zhang, *Electrochim. Commun.* **2013**, *37*, 96.
- [28] K. A. See, H.-L. Wu, K. C. Lau, M. Shin, L. Cheng, M. Balasubramanian, K. G. Gallagher, L. A. Curtiss, A. A. Gewirth, *ACS Appl. Mater. Interfaces* **2016**, *8*, 34360.
- [29] C.-W. Lee, Q. Pang, S. Ha, L. Cheng, S.-D. Han, K. R. Zavadil, K. G. Gallagher, L. F. Nazar, M. Balasubramanian, *ACS Cent. Sci.* **2017**, *3*, 605.
- [30] A. Nakanishi, K. Ueno, D. Watanabe, Y. Ugata, Y. Matsumae, J. Liu, M. L. Thomas, K. Dokko, M. Watanabe, *J. Phys. Chem. C* **2019**, *123*, 14229.
- [31] C. Weller, S. Thieme, P. Härtel, H. Althues, S. Kaskel, *J. Electrochem. Soc.* **2017**, *164*, A3766–A3771.
- [32] F. S. Reuter, C.-J. Huang, Y.-C. Hsieh, S. Dörfler, G. Brunklaus, H. Althues, M. Winter, S. D. Lin, B.-J. Hwang, S. Kaskel, *Batteries & Supercaps* **2021**, *4*, 347.
- [33] H. Lu, Y. Yuan, Z. Hou, Y. Lai, K. Zhang, Y. Liu, *RSC Adv.* **2016**, *6*, 18186.
- [34] P. Strubel, S. Thieme, T. Biemelt, A. Helmer, M. Oschatz, J. Brückner, H. Althues, S. Kaskel, *Adv. Funct. Mater.* **2015**, *25*, 287.
- [35] P. Strubel, H. Althues, S. Kaskel, *Carbon* **2016**, *107*, 705.
- [36] M. Thommes, K. Kaneko, A. V. Neimark, J. P. Olivier, F. Rodriguez-Reinoso, J. Rouquerol, K. S. W. Sing, *Pure Appl. Chem.* **2015**, *87*, 1051.
- [37] A. Espinola, P. M. Miguel, M. R. Salles, A. R. Pinto, *Carbon* **1986**, *24*, 337.
- [38] J. Sánchez-González, A. Macías-García, M. F. Alexandre-Franco, V. Gómez-Serrano, *Carbon* **2005**, *43*, 741.
- [39] a) A. C. Ferrari, J. Robertson, *Phys. Rev. B* **2000**, *61*, 14095; b) A. C. Ferrari, *Solid State Commun.* **2007**, *143*, 47.

- [40] M. Oschatz, P. Pré, S. Dörfler, W. Nickel, P. Beaunier, J.-N. Rouzaud, C. Fischer, E. Brunner, S. Kaskel, *Carbon* **2016**, *105*, 314.
- [41] S. Yoon, Y.-H. Lee, K.-H. Shin, S. B. Cho, W. J. Chung, *Electrochim. Acta* **2014**, *145*, 170.
- [42] P. Strubel, S. Thieme, C. Weller, H. Althues, S. Kaskel, *Nano Energy* **2017**, *34*, 437.
- [43] L. Kong, J.-X. Chen, H.-J. Peng, J.-Q. Huang, W. Zhu, Q. Jin, B.-Q. Li, X.-T. Zhang, Q. Zhang, *Energy Environ. Sci.* **2019**, *12*, 2976.
- [44] N. Azimi, Z. Xue, I. Bloom, M. L. Gordin, D. Wang, T. Daniel, C. Takoudis, Z. Zhang, *ACS Appl. Mater. Interfaces* **2015**, *7*, 9169.
- [45] C. Barchasz, F. Molton, C. Duboc, J.-C. Leprêtre, S. Patoux, F. Alloin, *Anal. Chem.* **2012**, *84*, 3973.
- [46] M. Piwko, C. Weller, F. Hippauf, S. Dörfler, H. Althues, S. Kaskel, *J. Electrochem. Soc.* **2018**, *165*, A1084-A1091.
- [47] E. Markevich, G. Salitra, Y. Talyosef, F. Chesneau, D. Aurbach, *J. Electrochem. Soc.* **2017**, *164*, A6244-A6253.
- [48] R. D. Rauh, F. S. Shuker, J. M. Marston, S. B. Brummer, *J. Inorg. Nucl. Chem.* **1977**, *39*, 1761.
- [49] Q. Pang, A. Shyamsunder, B. Narayanan, C. Y. Kwok, L. A. Curtiss, L. F. Nazar, *Nat. Energy* **2018**, *3*, 783.
- [50] L. Suo, Y.-S. Hu, H. Li, M. Armand, L. Chen, *Nat. Commun.* **2013**, *4*, 1481.
- [51] M. Cuisinier, P.-E. Cabelguen, B. D. Adams, A. Garsuch, M. Balasubramanian, L. F. Nazar, *Energy Environ. Sci.* **2014**, *7*, 2697.
- [52] a) M. Helen, M. A. Reddy, T. Dimant, U. Golla-Schindler, R. J. Behm, U. Kaiser, M. Fichtner, *Sci. Rep.* **2015**, *5*, 12146; b) L. Wang, Y. Lin, S. DeCarlo, Y. Wang, K. Leung, Y. Qi, K. Xu, C. Wang, B. W. Eichhorn, *Chem. Mater.* **2020**, *32*, 3765.
- [53] a) Z. Gong, Q. Wu, F. Wang, X. Li, X. Fan, H. Yang, Z. Luo, *RSC Adv.* **2016**, *6*, 37443; b) C. Fu, B. M. Wong, K. N. Bozhilov, J. Guo, *Chem. Sci.* **2016**, *7*, 1224; c) Z. Li, Y. Jiang, L. Yuan, Z. Yi, C. Wu, Y. Liu, P. Strasser, Y. Huang, *ACS Nano* **2014**, *8*, 9295.
- [54] U. Ulissi, S. Ito, S. M. Hosseini, A. Varzi, Y. Aihara, S. Passerini, *Adv. Energy Mater.* **2018**, *8*, 1801462.
- [55] W. Weppner, *J. Electrochem. Soc.* **1977**, *124*, 1569.
- [56] C. Xiong, T. S. Zhao, Y. X. Ren, H. R. Jiang, X. L. Zhou, *Electrochim. Acta* **2019**, *296*, 954.
- [57] a) L. Wang, T. Zhang, S. Yang, F. Cheng, J. Liang, J. Chen, *J. Energy Chem.* **2013**, *22*, 72; b) A. Andersen, N. N. Rajput, K. S. Han, H. Pan, N. Govind, K. A. Persson, K. T. Mueller, V. Murugesan, *Chem. Mater.* **2019**, *31*, 2308.
- [58] S. Thieme, J. Brückner, I. Bauer, M. Oschatz, L. Borchardt, H. Althues, S. Kaskel, *J. Mater. Chem. A* **2013**, *1*, 9225.

Manuscript received: November 23, 2020

Revised manuscript received: January 15, 2021

Accepted manuscript online: February 3, 2021

Version of record online: February 16, 2021